Tetracene ultrathin film growth on hydrogen-passivated silicon

Jens Niederhausen*‡, Rowan W. MacQueen, and Klaus Lips

Department ASPIN, Helmholtz-Zentrum Berlin für Materialen und Energie GmbH, Berlin, Germany

Hazem Aldahhak**‡, Wolf Gero Schmidt, and Uwe Gerstmann

Lehrstuhl für Theoretische Materialphysik, Universität Paderborn, 33095 Paderborn, Germany

Abstract

Inorganic-organic interfaces are important for enhancing the power conversion efficiency of silicon-based solar cells through singlet exciton fission (SF). We elucidated the structure of the first monolayers of tetracene (Tc), a SF molecule, on hydrogen-passivated Si(111) [H-Si(111)] and hydrogenated amorphous Si (a-Si:H) by combining near-edge X-ray absorption fine structure (NEXAFS) and X-ray photoelectron spectroscopy (XPS) experiments with density functional theory (DFT) calculations. For samples grown at or below substrate temperatures of 265 K, the resulting ultrathin Tc films are dominated by almost upright-standing molecules. The molecular arrangement is very similar to the Tc bulk phase, with only slightly higher average angle between the conjugated molecular plane normal and the surface normal (α) around 77°. Judging from carbon K-edge X-ray absorption spectra, the orientation of the Tc molecules are almost identical when grown on H-Si(111) and a-Si:H substrates as well as for (sub)mono- to several-monolayer coverages. Annealing to room temperature, however, changes the film structure towards a smaller α of about 63°. A detailed DFT-assisted analysis suggests that this structural transition is correlated with a lower packing density and requires a well-chosen amount of thermal energy. Therefore, we attribute the resulting structure to a distinct monolayer configuration that features less inclined, but still well-ordered molecules. The larger overlap with the substrate wavefunctions makes this arrangement attractive for an optimized interfacial electron transfer in SF-assisted silicon solar cells.

Introduction

Highly efficient (opto)electronic devices often rely on the rational combination of organic and inorganic materials. Conjugated organic molecules (COMs) exhibit efficient light-matter interactions while inorganic materials provide stability and efficient charge transport. The combination of tetracene (Tc) and silicon (Si) has received considerable attention in recent years due to Tc's potential to enhance the power conversion efficiency of Si-based solar cells: [1-3] The Tc molecules can undergo singlet fission (SF), a process which splits one singlet exciton into two triplet excitons [4]. SF can be exploited to produce additional photocurrent from energy which is ordinarily wasted during carrier thermalization in Si [5, 6].

The inorganic-organic interface is where particle and energy exchange between the two dissimilar materials takes place. Converting the tightly bound triplet excitons in Tc layers into current that can be extracted at the electrodes requires efficient exciton dissociation and/or Dexter energy transfer [7] at the Tc-Si interface. These processes proceed via interfacial electron transfer (IET) and therefore rely on the spatial proximity of the molecular and Si frontier electronic states. Since COMs like Tc have highly anisotropic electronic and chemical structures, their orientation at the interface is of particular importance to achieve an interface morphology that favors efficient IET. As an example, the IET-competing luminescence of Tc on an ultrathin alumina AlO_x layer on $Ni_3Al(111)$ is completely quenched if the molecules are planar or are at least only moderately inclined with respect to the surface, while the luminescence persists for larger Tc inclinations [8-10]. This behavior is attributed to the fact that a smaller Tc inclination gives rise to an increased

overlap of π orbitals (located above and below the planar Tc core) and the wave function tails of the metal states facilitating, thus, an efficient IET from Tc to the substrate.

In order to optimize IET-based devices, it is thus important to establish preparation protocols which lead to stable well-ordered molecular structures with favorable transport properties at the interface. Here, the orientation of the lowest layer plays a particularly important role. For Tc at non-terminated and therefore strongly interacting Si surfaces [11-13] interlayers with flat-lying molecules are reported. However, flat-lying interlayers establish a further, unfavorable intermolecular interface to the upright-standing molecules in the following layers [14]. An orientation of intermediate inclination thus might be more desirable. A more upright orientation is expected for weakly interacting surfaces.
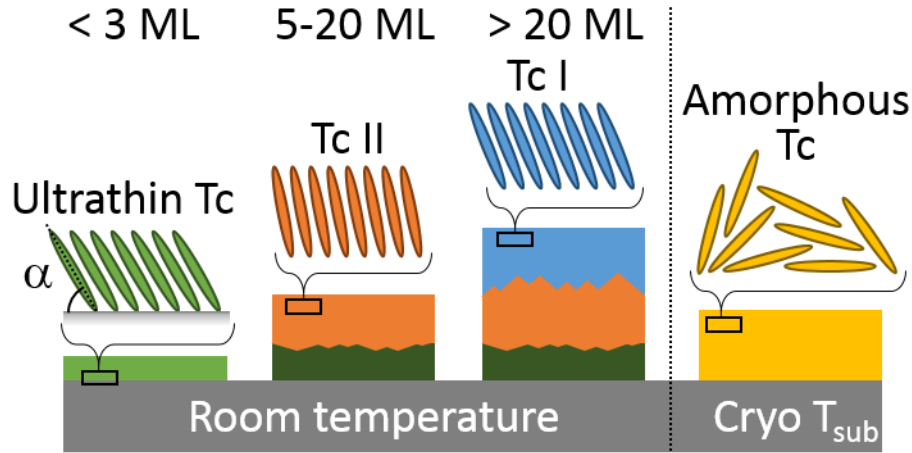

Figure 1: Schematic summary of Tc orientations for characteristic Tc films at weakly interacting substrates: Amorphous films form upon deposition at cryogenic T_{sub}. At room temperature, the largest well-ordered inclination is found in the so-called thin film phase (Tc II). Lower inclined molecules are found for the bulk phase (Tc I, > 20 ML) as well as for the ultrathin Tc phase (< 3 ML). The darker green indicates a structure transition upon completion of ~ the 3rd Tc ML observed in Refs. [15, 16]. The molecular inclination angle α is also indicated. Note that the Tc structures considered in this work feature two non-equivalent molecules in their unit cells (see Fig. 2). In this case, α refers to an average of the two angles as given by Eq. (2).

Tc structure formation has been widely studied on several different weakly-interacting surfaces, including H-Si [3, 15, 17-20], Si oxide [11, 16, 21-26], $AlO_x/Ni_3Al(111)$ [8, 9, 10], polystyrene, parylene C, polymethylmethacrylate, hexamethyldisilazane [27], Mylar© [28] evaporated carbon [29], and highly oriented pyrolytic graphite [30]. Thanks to the weak coupling to the substrates, the results are largely transferable. We summarize the current understanding schematically in Fig. 1. The molecular inclination is defined as the average angle between the conjugated molecular plane normal and the surface normal (α), as shown in Fig. 2. The smallest α for Tc on weakly-interacting surfaces (α ~43°) was reported in Ref. [10] for the non-luminescent Tc at $AlO_x/Ni_3Al(111)$, for which substrate temperatures, $T_{sub} < 100$ K during film growth was required. However, this growth mode leads to the formation of disordered films [8-10, 29] that are unfavorable for efficient charge and exciton transport as needed, e.g., in solar cell applications. In addition, disordered films of small molecules like Tc usually undergo drastic structural changes upon temperature increase to room temperature (RT). [9, 31, 32]. The use of cryogenic conditions during growth thus appears to be beneficial for decreasing the average Tc inclination angle α, but severely limits the applicability to device fabrication.

According to X-ray and low energy electron diffraction (XRD/LEED) measurements, Tc forms polycrystalline films when grown at non-cryogenic temperatures [8, 17, 18, 21-24, 33]. Two ordered phases have been reported (denoted Tc I and Tc II). Both phases feature rather upright-standing molecules, but with considerably different inclination angles α (see Fig. 2). Tc II is often referred as thin film phase since it was found to be predominant in Tc films between approximately 5 and 20-100 monolayers (ML) thick (depending on deposition rate and T_{sub}) on SiO_x [21-23, 33] and H-Si(111) [18]. Based on published crystal data, [23] α within standard thin films (Tc II) is 85.4°[1]. The unit cell of Tc I, in contrast, is measured to be close to that of bulk Tc ($\alpha = 74.5°$ [34]); it is thus called bulk-like and prevails in thicker films above 20-100 ML. The unit cells of Tc I and Tc II each consist of two non-equivalent molecules, as shown in Figure 2. The inclination of these molecules can be also described by the (average) angle between the molecular long axis (LA) and the plane of the underlying surface. This angle is denoted as α_{LA} and it differs much less for the two non-equivalent molecules than the inclination angle α, and thus helps further characterization of the investigated structures (see Fig. 2). However, one should bear in mind that while α_{LA} expresses a molecular inclination, its value is not comparable with α that is obtained from the NEXAFS measurements. This can be seen in Fig. 2 and was also discussed in Ref. [15]. The influence of two non-equivalent molecules existing in the unit cell on the effective inclination angle seen by NEXAFS is described by Eq. (2) and discussed more generally in Ref. [35].
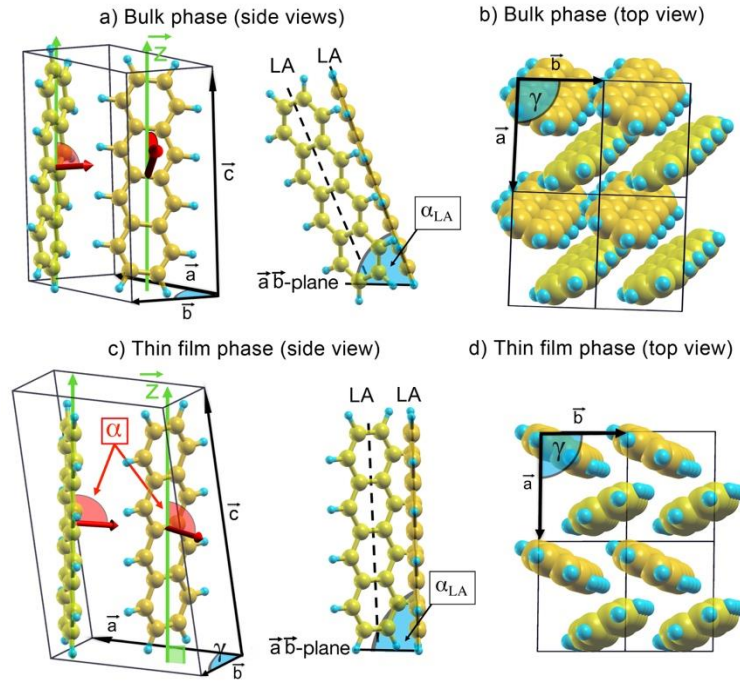

Figure 2 a)/c) side and b)/d) top-views for the experimentally determined structures of the tetracene bulk (Tc I, *top*) and thin film (Tc II, *bottom*) phases, published in Refs. [34] and [23], respectively. The parameters $\vec{a} = 0.781$ nm, $\vec{b} = 0.603$ nm and $\gamma = 94.208°$ ($\vec{a} = 0.756$ nm, $\vec{b} = 0.593$ nm and $\gamma = 90.10°$) define the lateral dimensions of the Tc I (Tc II) phases, whereby the unit cell of each phase includes two non-equivalent molecules. As guide to the eyes, the carbon atoms in the non-equivalent Tc within a unit cell are shown in slightly different colors. It is a unique feature of the bulk-phase that only one molecule is '*simply*' tilted, whereby the second molecule is tilted '*over the edge*', so that one

---

[1] We calculated the average α analytically according to Eq. (2) in order to obtain values comparable with those derived from NEXAFS.

of the two bottom H-atoms is considerably closer to the bottom of the unit cell (assumed to be the $\vec{ab}$-plane), see also a). With respect to this bottom $\vec{ab}$-plane, the two non-equivalent molecules show almost the same orientation α_{LA} for the long axis (LA), but differently rotated molecular planes. As a consequence, the average NEXAFS angle α between the molecular plane normal (red arrows) and the surface normal ($\vec{z}$-direction, green) deviates from α_{LA} (α is always larger than α_{LA}). In the thin film phase, the inclination of the two molecules is at least qualitatively identical. Thereby, Tc II exhibits denser morphology and the Tc molecules are more inclined with respect to the $\vec{ab}$-plane ($\alpha_{LA} = 85.4°$ instead of $69.48°$ in Tc I).

In Tc films consisting of only a few ML, α values of $78°$ and below, i.e. inclination angles similar to Tc-bulk, have been reported, with a clear trend to much smaller α around $63°$ for coverages of approximately 1.2 ML or below [10, 11, 15]. Notably, ex-situ atomic force and scanning tunneling microscopy (AFM/STM) revealed that Tc islands with a complete third ML on H-Si(100) [15] and SiO$_2$ [16] show structural characteristics clearly distinct from thinner (1-2 ML) films: They appear to be denser [15] and more stable against interlayer diffusion [16]. Consistently, in situ, real-time grazing incidence XRD found that the crystal structure of Tc films on SiO$_2$ changes within the first few (1-4) MLs [33], suggesting the existence of a proper, but so far not well established ultrathin Tc phase.

The structure of the molecules in Tc films depends not only on the film thickness, but also, and sometimes more decisively, on T_{sub} [9, 24]. Ref. [9] reports structural changes related to changing molecular orientation at around $T_{sub} = 210$ K; changes around $T_{sub} = 250$ K and 280 K were interpreted as island formation and partial ordering within the islands, respectively. Significant desorption starts at temperatures of approximately RT [8]. When heating single-crystalline Tc, a phase transition from Tc II to Tc I occurs around 275 K [36].

In this combined experimental and theoretical work, we study the molecular arrangement at the Tc/H-Si interface for ultrathin films (1 to ~3 ML thickness), for which the reported experimental observations, although decisive for IET, are by far not sufficiently well understood. For this purpose, near-edge X-ray absorption fine structure (NEXAFS) measurements supplemented by DFT calculations are applied. By using single-crystalline silicon H-Si(111) and amorphous silicon (a-Si:H) as substrates, we investigate possible template effects [37]. We also investigate the influence of coverage/film thickness. However, the main focus is on the substrate temperature T_{sub} during and after Tc film growth. This parameter controls dewetting, desorption, and phase transitions, and is thus critical for preparing well-defined ultrathin Tc film morphologies.

In the following, we show that (*i*) a hydrogen-terminated Si surface entails weak interaction between Tc and the substrates, (*ii*) the molecular arrangement in ultrathin Tc-films (~1 ML regime) is highly sensitive to the local molecular coverage, and (*iii*) heating an ultrathin Tc film to room temperature induces a transition to a meta-stable phase with lower density and intermediate molecular inclination angles. Finally, we discuss our data with regard to controlling the molecular inclination at Si-Tc interfaces.

Materials and Methods

Sample Preparation

The substrates, c-Si(111) (cleaned via the RCA process developed by the Radio Corporation of America) with a native oxide or a-Si:H layers grown via plasma-enhanced chemical vapor deposition on glass substrates, were cleaned by short immersion into dilute hydrofluoric acid (1% HF, 2 min) and subsequently transported and loaded under N$_2$ into the ultra-high vacuum (UHV)

system. The air exposure during sample mounting was ≤ 1 min. Tc deposition was conducted in-system, with no break in UHV conditions between deposition and measurement. Tc films were deposited in the preparation chamber from a Knudsen cell at rates of 0.13–0.5 nm/min as calibrated with a quartz crystal microbalance. Nominal thickness values relate to this rate calibration. The substrates were cooled during deposition and also during measurement in the analysis chamber. A brief increase in cooling power was applied prior to transfer between the two chambers to ensure that no positive spike in temperature occurred.

The Tc deposition conditions are summarized in Table 2. Typically, Tc deposition was carried out at $T_{sub} = 265$ K. One sample, H-Si(111) No. 1, was annealed to T = 720 K for 70 min in the UHV chamber to minimize the presence of adventitious carbon contamination [cf. Fig. 7 a)], then cooled to $T = 200 \pm 50$ K[2] for Tc deposition. The Tc film for these conditions was ordered but showed no sign of interlayer diffusion. Its growth mode thus differs qualitatively from that of samples held at T = 265 K during growth. We denote this deposition regime as low temperature (LT).

NEXAFS and XPS

The experiments were performed at the HE-SGM beamline at the synchrotron radiation facility BESSY II, which is part of Helmholtz-Zentrum Berlin für Materialen und Energie GmbH (HZB).

The average molecular inclination angle α can be determined from the θ-dependence of the NEXAFS spectral intensity $I_\alpha(\theta)$. [38] Assuming at least three-fold axial symmetry, $I_\alpha(\theta)$ becomes a function of θ alone:

$$I_\alpha(\theta) = 1/2\ (3P\cos^2\theta - 1)\cos^2\alpha + 1/2(1 - P\cos^2\theta) \tag{1}$$

The polarization factor of the p-polarized X-ray beam (P) was 0.91±0.01. NEXAFS spectra were measured in partial electron yield (PEY) mode with a retarding voltage of −150 V using a custom-made multichannel detector. The X-ray incidence angle (θ) is defined as the angle between the wave vector of incident X-rays and the surface plane of the substrate [see inset in Fig. 9 a)]. We estimate a θ uncertainty of 0.5°.

Note that $I_\alpha(\theta)$ is not linear in α and the arithmetic average of $I_\alpha(\theta)$ collected in the NEXAFS measurements does not exactly translate into the arithmetic average of α. In this work, we deal with a 1:1 ratio of two non-equivalent molecules with angles α_1 and α_2. This yields $I_\alpha = (I_{\alpha_1} + I_{\alpha_1})/2$ and the NEXAFS-derived average inclination angle

$$\alpha = \cos^{-1}\sqrt{(\cos^2\alpha_1 + \cos^2\alpha_1)/2} \tag{2}$$

The X-ray photon energy scale in the NEXAFS experiments was calibrated by means of a carbon contaminated gold mesh upstream from the sample position that exhibit a characteristic and previously calibrated absorption peak [35, 39]. The raw PEY signal was corrected for the known spectral intensity distribution of the HE-SGM beamline.

X-ray photoelectron spectroscopy (XPS) data were collected with a Scienta R3000 hemispherical electron analyzer employing 700 eV, 350 eV, and 153 eV photon energies for survey, Si 2p, and valence electron regions, respectively. We determine the overlayer thickness (d) from the XPS

---

[2] The thermocouple was positioned without direct contact to the sample, so that the actual T_{sub} remains less defined than for the other samples. T_{sub} should be substantially lower than the 265 K registered by the thermocouple, but still above the transition between disordered and upright-standing molecules, which we expect somewhat below $T_{sub} = 200$ K observed for AlO$_x$/Ni$_3$Al(111) [9].

intensities (I) measured for C 1s (Tc and carbon contaminants) and Si 2p under the same excitation conditions (constant X-ray intensity and energy). Note that this approach assumes a homogenous film thickness. In the case of rough films, d is smaller than the real average film thickness and larger than the minimum film thickness. When using I ratios, we have to consider only the following proportionalities: $dI \propto \sigma D T \exp(-x/EAL) dx$. The photoionization cross sections σ were taken from Ref. [40] and the atom densities, $D_{Tc} = 63$ nm^{-3} [34] and $D_{Si} = 50$ nm^{-3} [41], were determined from reported crystal structures. T is the transmission function of the spectrometer [42]. We use the effective attenuation length (EAL) *for quantitative analysis*, which replaces the inelastic mean free path in formulae derived for quantitative XPS analyses on the assumption that elastic-scattering effects were negligible [43]. Both T and EAL depend on the photoelectron kinetic energy. For a Tc layer of thickness d:

$$I_{Tc} \propto \int_0^d \sigma_{Tc} D_{Tc} T_{Tc} e^{-x/EAL_{Tc}} \, dx = \sigma_{Tc} D_{Tc} T_{Tc} EAL_{Tc}(1 - e^{-d/EAL_{Tc}}) \tag{3a}$$

$$I_{Si} \propto \int_d^\infty \sigma_{Si} D_{Si} T_{Si} e^{-x/EAL_{Si}} \, dx = \sigma_{Si} D_{Si} T_{Si} EAL_{Si} e^{-d/EAL_{Si}} \tag{3b}$$

No algebraic solution for d is possible and we solved each experimental I_{Tc} to I_{Si} ratio for d numerically.

Theoretical Methods

For an as realistic as possible modeling of the investigated Tc monolayer structures on H-Si(111) surface, the molecular species together with the substrates have been calculated using periodic boundary conditions. The H-terminated surface (see Fig. 3 left) has been modeled by a slab containing four Si bilayers separated by a vacuum with a thickness of 25 Å; i.e., a monolayer of H atoms saturates the dangling bonds in the topmost Si layer. The bottom atoms were also terminated by H atoms and frozen at the ideal lattice sites. The adsorbate structures have been relaxed using density functional theory (DFT) calculations with the Quantum ESPRESSO package (QE) [44]. The PBE functional [45] complemented with dispersion correction (DFT-D) [46] was used to model the electron exchange and correlation. Using the DFT-D approximation, our calculations predict the bulk lattice constants of Si within an error bar less than 0.5%. The calculated lattice parameter has been used as a basis for the slab models. Norm-conserving pseudopotentials were used to describe the electron-ion interactions. As basis functions, plane waves up to a cutoff energy of 60 Ry were used. Convergence criteria of 10^{-4} eV/Å for the maximum final forces and 10^{-8} eV for the total energy were used. The gauge including (GI-PAW) pseudopotential scheme was used to calculate the spectroscopic X-ray fingerprints of the Tc I and Tc II crystal structures as well as different adsorbate structures on H-Si(111). Specifically, we employed the Xspectra code [47, 48] of QE to calculate the NEXAFS C K-edge. To model the 1s core hole, scalar-relativistic multiprojector GIPAW pseudopotentials with a corresponding occupation of the inner shells were generated. This approach yields reliable results [49, 50], and is computationally very efficient in describing excitonic effects [51].

The Lanzcos recursion scheme was employed to expand the Green's function of the empty states (continued-fraction expansion) [52-54], allowing for the calculation of the XAS cross sections. By employing this procedure, the near- and far-edge features of the absorption spectrum can be reliably described [55-58]. As quadrupole contributions are very small and restricted to the pre-edge region, we focused on the dipole-contributions. The XAS cross sections of each carbon atom were calculated in a 40 eV range above the respective K-edge. Then, the total NEXAFS spectrum of the molecular system was obtained from the superposition of the individual spectra offset by the corresponding core-level shifts, calculated within DFT [59-62] for each carbon atom (see e.g., Refs.

[49, 50, 63, 64] for further details). For structures with axial symmetry, the XAS cross section (σ_{XAS}) for an *E*-field component, tilted by an angle θ with respect to the surface normal, can be accurately calculated by averaging over two orthogonal azimuthal orientations (for an arbitrary angle φ_0):

$$\sigma(\theta) = 1/2 \; [\sigma_{XAS}(\theta, \varphi_0) + \sigma_{XAS}(\theta, \varphi_0 + 90°)] \tag{4}$$

In the present case, the threefold symmetry of the substrate is broken by the attached molecules. To account for the enhanced variation with φ, we thus considered at least four different azimuthal cases (also $\varphi_0 + 45°$ and $\varphi_0 + 135°$) while determining the angular averaged spectra. The spectra were then aligned to the respective experimental K-edges. The linewidth was energy-dependent, [65] rising arctan-like from 0.1 eV at 280 eV to 1.0 eV at 320 eV.

Results

DFT-analysis of molecular structure of first monolayer

First-monolayer structure of Tc on H-Si(111).

Since the experiments do not provide an atomic registry between the Tc film and the substrate lattice, a variety of possible surface supercells with different size, shape, and molecular coverage within each cell, have been probed by DFT total energy calculations. Within each of the calculated structures, we allowed the starting configurations of Tc to have different possible inclination angles with respect to the surface normal and different azimuthal orientations before they were completely relaxed.
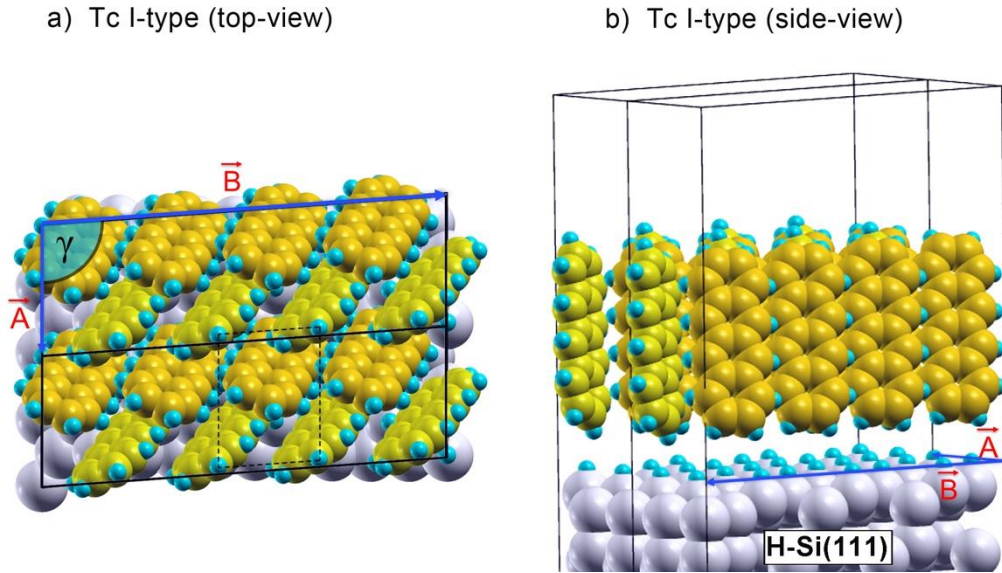

Figure 3: Modelling an ideal Tc monolayer (in LT regime): a) and b): top- and side-views, respectively, of the DFT-calculated *most stable* monolayers of Tc molecules at H-Si(111), denoted as Tc I-type monolayers. $\vec{A}$, $\vec{B}$, and the angle γ define the lateral supercell used to model the structure: $\vec{A} = 0.772$ nm, $\vec{B} = 2.370$ nm and $\gamma = 94.21°$ resembling 1×4 repetition of the crystalline unit cells (dashed lines). The corresponding epitaxy matrix is given by $\begin{pmatrix} A_{Tc\,I\,-\,type} \\ B_{Tc\,I\,-\,type} \end{pmatrix} = \begin{pmatrix} 2 & -2 \\ 3 & 4 \end{pmatrix} \begin{pmatrix} x_1 \\ x_2 \end{pmatrix}$, where $\vec{x}_1$ and $\vec{x}_2$ indicate the primitive vectors of the Si(111) surface. The carbon atoms of the two non-equivalent Tc molecules within a unit cell are shown in slightly different colors.

According to our total energy calculations, the most stable monolayer structure features properties close to the Tc I (bulk) phase, whereby eight Tc molecules are included within a (1×4) superstructure (see Fig. 3). In the following, we denote this structure as Tc I-type. Furthermore, to simplify the discussion of the lateral dimensions, we denote the area of the $\vec{ab}$-plane of the Tc I unit cell [see Fig. 2 b)] as A_{TcI} and use it as reference for all other structures. Apart from the 1×4 superstructure, the density of the Tc I-type surface cell (dashed lines in Fig. 3) is close to that of the crystalline Tc I unit cell and the area per molecule is 97% of A_{TcI}. The two non-equivalent types of Tc molecules show the characteristic aspects of the Tc I phase (one molecule is 'simply' tilted, while the second, shown in slightly lighter colors, is tilted 'over the edge') and the angles $\alpha_{LA} = 67.5°$ and $\alpha = 73.5°$ are close to, but still distinct from those derived from the XRD data for crystalline Tc I (bulk) [34] ($\alpha_{LA} = 69.5°$ and $\alpha = 74.5°$). Such differences have to be expected, since the modelled monolayer experiences a weak, but direct interaction with the substrate, not present in the Tc I (bulk) unit cells. The total-energy calculations yield an adsorption energy of -1.27 eV (per Tc molecule) for the Tc I-type adsorbate structure, which is higher by 0.52 eV than the adsorption energy for a single flat-lying molecule (see also Table 1). In comparison with a single upright standing Tc even 1.07 eV are gained showing that intermolecular interaction is predominantly responsible for the stability of the Tc I-type monolayer. We briefly note that the calculations found no stable side-on monolayer of Tc which holds the characteristic herringbone structures. All tested structures of this kind finally result in a flat-lying geometry.

Table 1: Adsorption energies per a Tc molecule (E_{ads}) calculated for the structures shown in Figs. 4, 3, 6. *Note that the so-called on-side geometry is only stable assuming Cs symmetry with the molecular plane as mirror plane, preventing the structure from 'falling down' to a flat-lying geometry. All ML consist of rather upright standing molecules. A comparison with the respective single Tc absorption shows that the stability of the ML is predominantly (70...85%) due to intermolecular interaction.

Structure		E_{ads} [eV]
single Tc molecules on H-Si(111)	Flat-lying	-0.75
	On-side	-0.35*
	Upright standing	-0.20
ML of Tc molecules on H-Si(111)	Tc I-type	-1.27
	Tc II-type	-1.20
	Tc Ib-type	-1.10

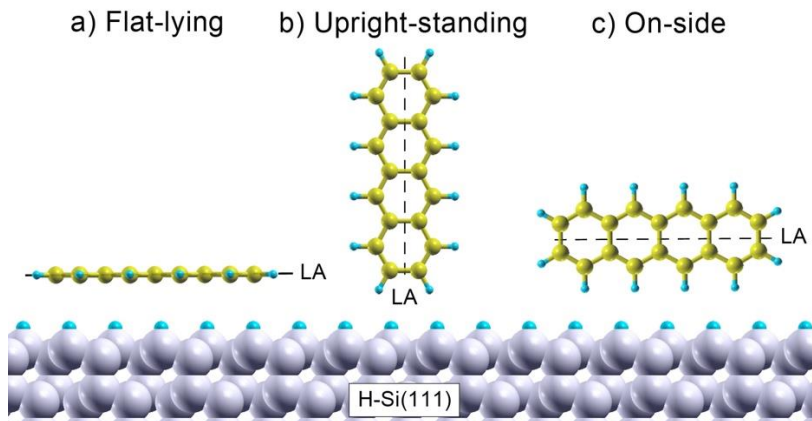a) Flat-lying   b) Upright-standing   c) On-side

Figure 4: Variety of possible adsorption geometries of single Tc on H-Si(111). In the a) flat-lying [b) upright standing] geometry, both the long molecular axis (LA) as well as the molecular plane are parallel [perpendicular] to the surface plane. In the on-side geometries, the molecular plane is perpendicular to the surface plane, while LA is parallel to it. For further details, see also Table 1.

Relation between Tc inclinations and unit cell dimensions

In order to report on the changes of the Tc inclination upon variation of the local molecular coverage, we assess the related changes of the total energy and molecular orientation within a Tc monolayer. Since we have to compare our results with the NEXAFS measurements, besides α_{LA} we report also the value of the NEXAFS inclination angle α. In order to circumvent misleading, non-continuous strain effects within the substrate, these calculations are performed initially without substrate and belong, thus, to a completely unbound (free) Tc-monolayer. In the light of our total energy calculations (see Table 1), this appears to be a reasonable approximation, at least for dense monolayers. For the free monolayer, the total energy minimum is still found around 97 % of A_{TcI}, while providing $\alpha_{LA} = 68.5°$ and $\alpha = 73.8°$, in nearly perfect agreement with the values (67.5° and 73.0°) calculated for the Tc I-type monolayer at H-Si(111), see also Fig. 3. The Tc-substrate interaction only weakly affects the molecular inclination, and does not change the calculated trend considerably.
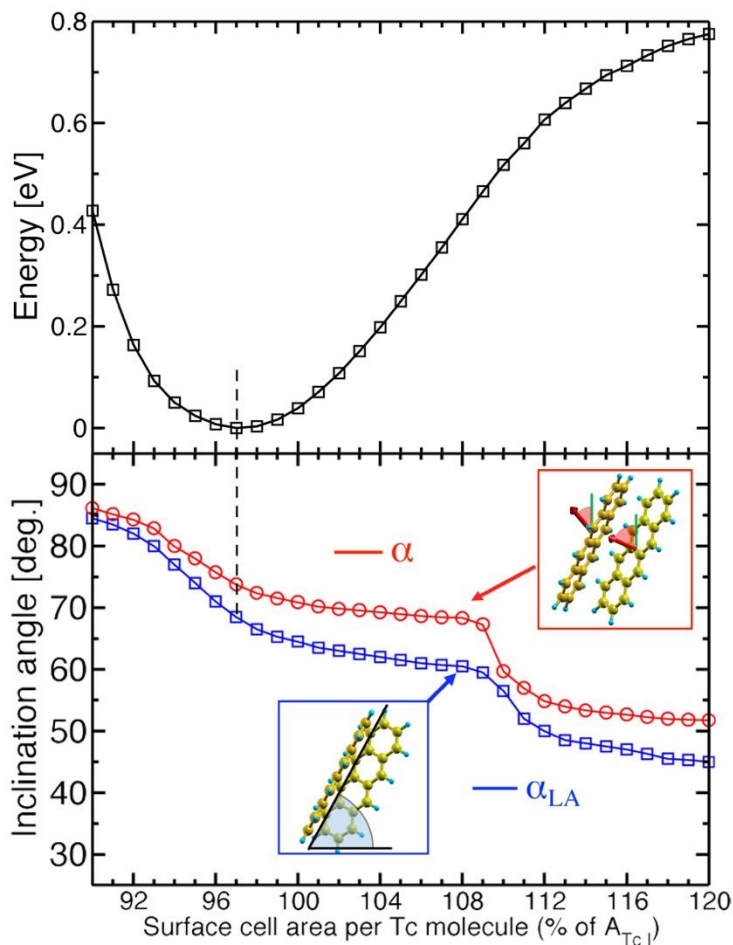

Figure 5: (*top*): Total energy for Tc monolayers as function of the surface unit cell area per molecule, referenced to that of bulk-Tc (A_{TcI}). The energy minimum is at 97% of A_{TcI}, as in case of the Tc I-type structure shown in Fig. 3. (*bottom*): Corresponding geometric inclination angle α_{LA}, defined by the average orientation of the molecules' long axis (LA) against the surface plane. Note that α_{LA} is different from α determined from the

NEXAFS analysis, which is also included. For increasing lateral cell size to about 130%, α_{LA} goes slightly down to about 40°, before for even lower coverage more individual arrangements in pairs or even flat-lying molecules are preferred.

Fig. 5 shows the calculated inclination angles as a function of unit cell size. Allowing the molecular tilting and also the herringbone angle to relax, the calculations found that both angles, α_{LA} as well as α, decrease with increasing cell size, i.e. as expected, the Tc molecules tend to be more planar for locally lower molecular coverages, while keeping the herringbone structure.[3] In the range between 90 % and 108 % A_{TcI}, the decrease of α_{LA} and α is almost *arccot*-like, smoothly approaching $\alpha_{LA} = 60°$ for 108%. Notably, this flattening of the molecules reflects the effect experimentally observed [15, 11]. We will come back to this point later in the experimental part. Around 110 % surface area, a qualitative change of the molecular arrangement yields a sudden decrease of the inclination angle by about 10° allowing the Tc molecules to adapt more planar geometries. Decreasing the lateral dimensions to about 90% of A_{TcI}, on the other hand, yields more inclined molecules which resembles those of Tc II (thin film) structures.

To explore the influence of the substrate, we determined the stable structures of Tc molecules in supercells of lateral dimension larger and smaller than the Tc I-type monolayer by about 10%, whereby the lattice vectors have to be chosen to fit to the underlying substrate. In both cases the molecules are again arranged in a herringbone structure. Figure 6 a, c) shows a surface cell forming a 1×5 repetition of unit cells, where the area per molecule is now 89% of A_{TcI}. It includes ten upright standing Tc molecules ($\alpha_{LA} = 88°$ and $\alpha = 88.2°$) and resembles the thin film phase [23]. This monolayer structure is thus denoted as Tc II-type. Figure 6 b, d) provides an example for a less dense arrangement, whereby the area per molecule is 110% of A_{TcI}. It shows a simple, rectangular 1×1 superstructure. Similar to the Tc I-type it resembles the Tc-bulk molecular arrangement, but without adapting an oblique unit cell ($\gamma = 90°$). It will be thus denoted as Tc Ib-type in the following. In comparison with the Tc I-type, the Tc molecules in the less dense Tc Ib-type structure show a smaller inclination angle $\alpha_{LA} = 63°$. Since the angle between the conjugated molecular plane and the surface normal of the second Tc molecule (which is tilted 'over the edge') is about 76°, the average NEXAFS α for this structure is about 68.5°, again considerably smaller than the value obtained for the Tc I-type arrangement.

---

[3] Previous studies reported that a decrease of the local coverage enhances the importance of the molecule-surface interaction and favors smaller molecular inclinations [66-68].
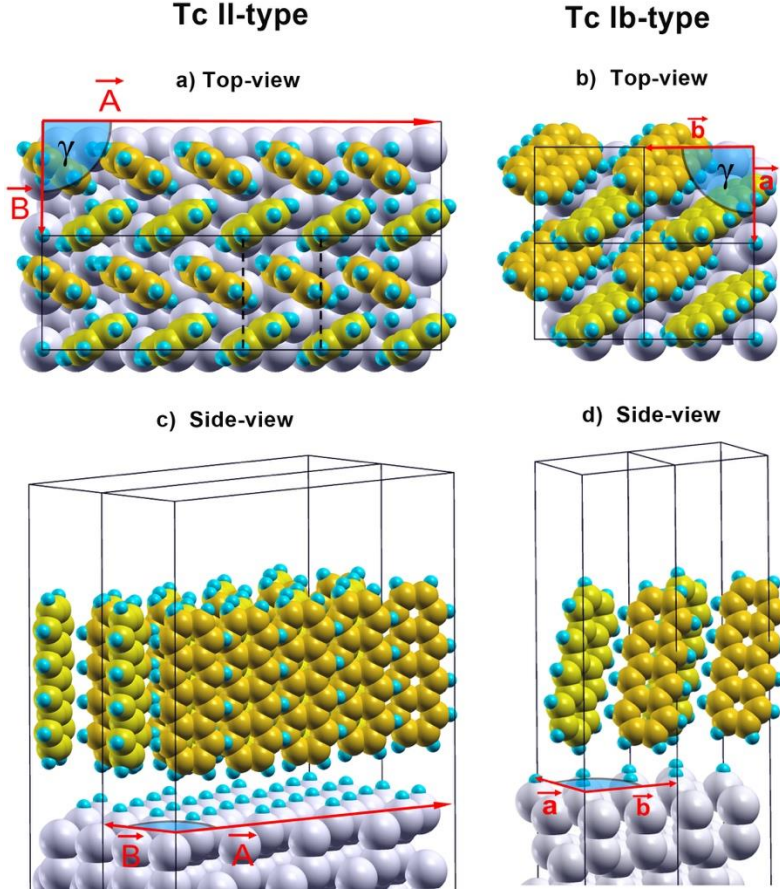
Figure 6: *a*) [b)] Top and c) [d)] side-views of the geometries of a Tc monolayer calculated in rectangular supercells of lateral dimensions $\vec{A}$ = 0.772 nm, $\vec{B}$ = 2.702 nm [$\vec{a}$ = 0.675 nm, $\vec{b}$ = 0.772 nm] and γ = 90°, resembling 1×5 [1×1] unit cell reconstructions for Tc II-type [Tc Ib-type], respectively. These structures represent 10% more dense (Tc II-type) and 10% less dense coverage (Tc Ib-type) in comparison to the most stable Tc I-type structure shown in Fig. 3. The corresponding epitaxy matrices are given by $\begin{pmatrix} A_{Tc\,II\,-\,type} \\ B_{Tc\,II\,-\,type} \end{pmatrix} = \begin{pmatrix} 2 & -2 \\ 4 & 4 \end{pmatrix} \begin{pmatrix} x_1 \\ x_2 \end{pmatrix}$ and $\begin{pmatrix} a_{Tc\,Ib\,-\,type} \\ b_{Tc\,Ib\,-\,type} \end{pmatrix} = \begin{pmatrix} 1 & 1 \\ 2 & -2 \end{pmatrix} \begin{pmatrix} x_1 \\ x_2 \end{pmatrix}$, where $\vec{x}_1$ and $\vec{x}_2$ again indicate the primitive vectors of the H-Si(111) substrate.

Possible influence of kinetic effects

The total-energy calculations yield an adsorption energy per Tc molecule of -1.20 (-1.10) eV for Tc II (Tc Ib)-type structures, as expected slightly lower than for the Tc I-type monolayer (-1.27 eV). This indicates that the formation of the Tc I-type monolayer on H-Si(111) is most favorable. However, in case of the Tc-II type structure, this assessment is reverted when including its higher areal density. The adsorption energy per nm^2 is 0.578 meV and, by this, ~4% larger than for the Tc-I type monolayer (0.555 meV). This effect suggests that kinetic effects during and after film growth [16, 19, 25] will influence whether preferentially Tc I or Tc II-type (thin film-like) molecular arrangement form. In addition, at elevated temperatures, vibrational and configurational entropy contributions to the adlayer free energy will modify the energetics. Their explicit treatment is beyond the scope of this work, but temperature effects can be implicitly taken into account via their influence on molecular coverage. In the following sections, we investigate the crucial role of the temperature to initiate structures deviating from the most stable ground state configuration, so that arrangements with intermediate molecular inclinations like, e.g., Tc Ib-type become possible.

11

With the theoretical predicted characteristic angles as a function of local Tc coverage at hand, we set out to determine experimentally the orientation of the first monolayer as a function of coverage and temperature.

Substrates characterization

We used the HF-dipped substrates either as loaded [H-Si(111) (No. 2) and a-Si:H] or after annealing at 720 K for 70 min in the vacuum chamber [H-Si(111) (No. 1)], thereby reflecting realistic device fabrication conditions. To check the effectiveness of these cleaning procedures, we first determined the amount of adventitious carbon and surface oxide. The inset in Fig. 7 a) shows the C 1s region for an as-loaded H-Si(111) sample (dashed gray line). A corresponding NEXAFS C K-edge spectra can be found in Fig. 10 b). The black spectrum in Fig. 7 a) presents a XPS survey spectrum of the same substrate immediately after annealing and shows a much smaller C 1s signal. Analyzing the data with Eq. (3), we find that the annealing reduced the carbon contamination by about 80%. Fig. 7 b) presents the Si 2p region for H-Si(111) after annealing and for a-Si:H. Minor sub-stoichiometric oxide signals can be seen. The a-Si:H sample also exhibits a small SiO_2 contribution. The traces of Si oxide and oxygen containing adventitious carbon can explain the O 1s signal in the survey spectrum of Fig. 7 a).
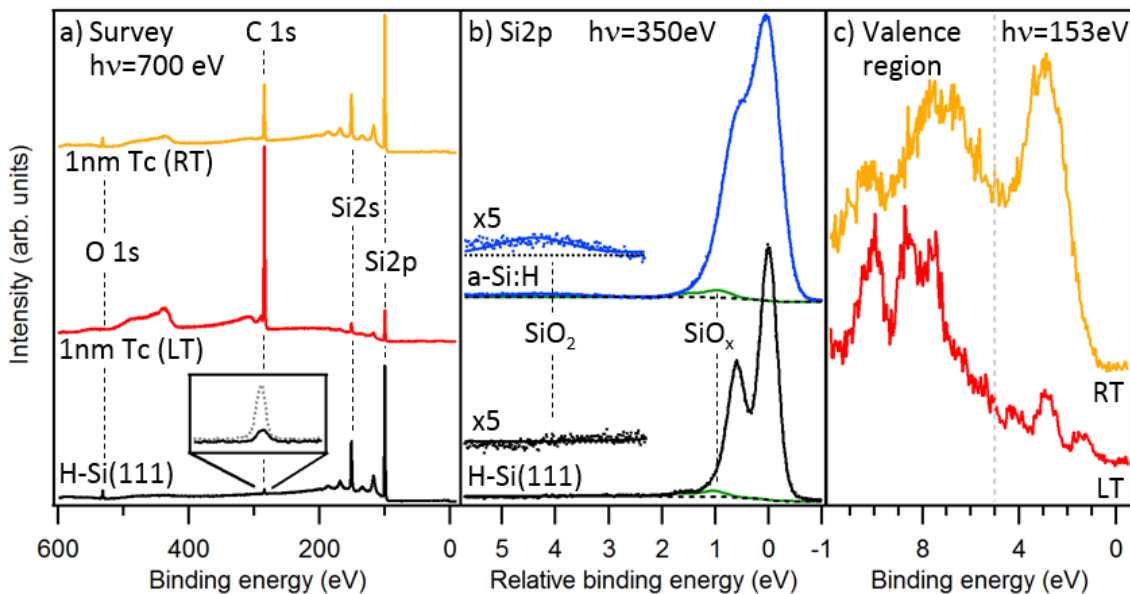
Tc films grown and measured at LT

Fig. 7: a): XPS survey spectra of H-Si(111) before and after Tc deposition at LT as well as upon warming the Tc to room temperature (RT). The inset shows a close-up of the C 1s region and includes a spectrum of the substrate before annealing (gray dotted line). The annealed H-Si(111) substrate (720 K for 70 min, black) still features C 1s and O 1s intensity from substrate contamination not completely removed by the annealing. The red spectrum belongs to a Tc film of nominally 1 nm coverage deposited and measured at LT; the yellow spectrum was measured after warming up to room temperature (RT). Note (*i*) the increase of the C 1s signal upon Tc deposition and the corresponding decrease in Si 2p and Si 2s, and (*ii*) the opposite trend upon raising the temperature to RT. b): The Si 2p region for H-Si(111) after annealing (black) and a-Si:H (blue). The binding energy scale is referenced to the Si $2p_{3/2}$ peak maximum. Only small (~3%) sub-stoichiometric oxide contributions (green) are observed. Traces of SiO_2 (~2%) can be resolved for a-Si:H, but not for H-Si(111). c): The valence electron region for the same Tc film as in a). For the cooled sample (red), the spectrum is dominated by the Tc molecular orbitals. Upon exposure to room temperature (yellow) the spectrum becomes dominated by the Si bands. The spectral regions above and below 5 eV (indicated by the vertical dotted line) were acquired with different statistics.

12

Table 2: Summary of the preparation and measurement conditions of the investigated samples and the film properties derived from XPS and NEXAFS. The minimum average film thickness (d) is corrected by subtracting the d_0-value of the residual substrate-related carbon species. Both values were derived from Eq. (3). A systematic error of 30% is estimated due to the large uncertainty of the electron attenuation lengths in COM films [69] and the fact that our analysis relies on the ratio of two core levels with a 135 eV difference in binding energy. The fitted inclination angle of Tc (α) based on NEXAFS analysis is also given. The table reports only the α error that stems from the numerical fitting with Eq. (1) and estimated uncertainties in fitting the NEXAFS spectra. An additional systematic error due to uncertainties of θ and P amounts to 1° for α in between 75° and 79°. This error is insignificant for the smaller α values found for the RT sample. Note that due to the lower T_{sub}, H-Si(111) (No. 1) exhibits a different growth mode than the other samples. In addition, that the H-Si(111) (No. 2) with nominal 3 nm coverage likely corresponds to a different film thickness regime than the other films (c.f. Fig. 1)

Sample	Nominal coverage (nm)	Rate (nm/min)	T_{sub} (K)	d_0 (nm)/ d (nm)	α (°)
H-Si(111) #1	0	-	RT	0.05 / 0.00	
	1	0.38	LT	3.30 / 3.25	76.3±1
	1	-	RT	0.55 / 0.50	62.7±2
H-Si(111) #2	0	-	RT	0.20 / 0.00	
	1	0.20	265	1.35 / 1.15	77.8±1.5
	2	0.45	265	0.70 / 0.50	78.5±1.5
	3	0.50	265	0.80 / 0.60	76.6±1.5
a-Si:H	0	-	RT	0.30 / 0.00	
	1	0.13	265	1.60 / 1.30	76.3±1.5
	2	0.50	265	1.35 / 1.05	77.5±1.5

We first look at Tc/H-Si(111) grown with T_{sub} sufficiently high for an ordered film to be formed and sufficiently low to prevent any significant dewetting, thus resulting in a (in the best case) closed and ultrathin Tc film. To that end, the substrate that had undergone UHV-annealing at 720 K was cooled to LT for Tc film growth and subsequent analysis. A Tc film of 1 nm nominal coverage was deposited onto H-Si(111) and then transferred to the analysis chamber without significantly raising the sample temperature. This sample was also used for the measurements with the film at room temperature presented later.

In the valence band region, shown in Fig. 7 c), features derived from Tc's molecular orbitals dominate the spectrum. The EAL[4] in COMs for electrons with 153 eV kinetic energy is 0.6–1.0 nm [43, 69]. Accordingly, the observed suppression of Si-related spectral intensity to $< 10\%$ its original value implies that a *closed* Tc film of at least 1.4 nm average height was formed. As shown in Fig. 7 a), the Si 2p and 2s signals were greatly reduced following Tc deposition, while the C 1s signal was increased. The minimum average Tc film thickness d can be derived from the Si 2s to C 1s XPS intensity ratio by means of Eq. (3). This yields $d = 3.25\pm1$ nm (*cf.* Table 2). The deviation from the nominal thickness of 1 nm is likely due to the sticking coefficient of H:Si(111) at LT being significantly higher than that of the quartz crystal microbalance kept at room temperature. As will be discussed below, Tc adopts an upright-standing orientation with a monolayer thickness

---

[4] Different from the more common inelastic mean free path, the *EAL* also accounts for elastic-scattering effects.

(ML) of 1.0 – 1.3 nm in all films investigated in this work. Accordingly, *d* translates to 2.8±1 ML. From our quantitative analysis we can thus infer a closed first monolayer and a second monolayer that is at least predominately closed. We can furthermore conclude that cooling the substrate to LT effectively suppressed dewetting of the first Tc monolayer. This behavior resembles the Frank–van der Merwe growth mode and is illustrated in Fig. 8 a).
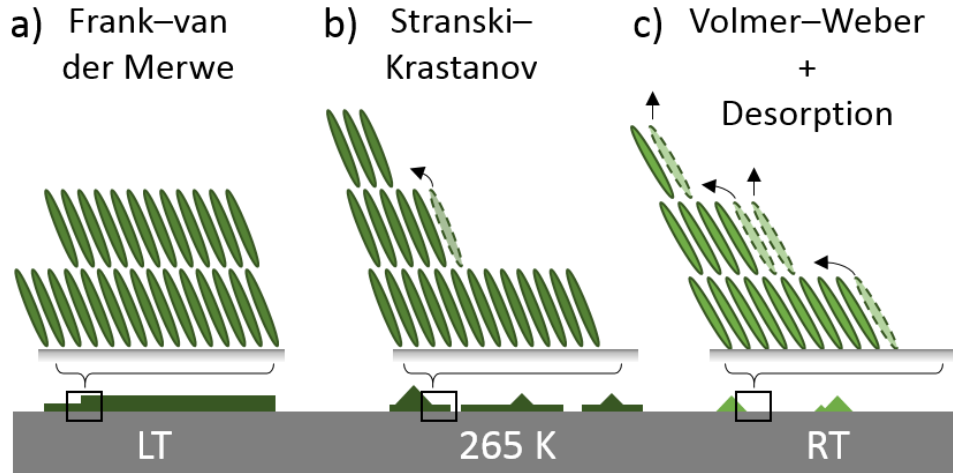

Figure 8: Schematic summary of Tc growth modes encountered in this work. a) When Tc is deposited at LT, interlayer diffusion is completely absent, giving rise to Frank–van der Merwe (layer-by-layer) growth. b) For Tc grown at 265 K, interlayer diffusion occurs predominantly for layers beyond the first monolayer, akin to Stranski–Krastanov growth. c) At RT, also the first monolayer undergoes interlayer diffusion at high rates, leading to Volmer–Weber-type growth where 3D island formation consumes all Tc material. In addition, at RT significant Tc desorption takes place under UHV conditions.
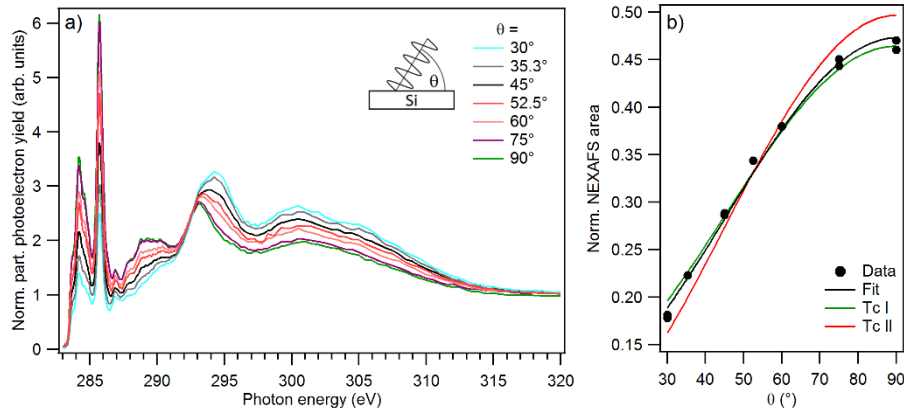

Figure 9: a): C K-edge NEXAFS spectra (for different angle of incidence θ, see inset) for a nominally 1nm-thick ultrathin Tc film at H-Si(111) grown and measured at LT. b): The π^* resonance intensities derived from the spectra shown in a) as a function of θ, a fit to the data according to Eq. (1), and the expected curves for pure Tc I (bulk) and Tc II (thin film) crystal phases. (Error bars are within the size of the symbols).

To characterize the spectral signature and the conformational properties of the LT Tc film, C K-edge angular resolved NEXAFS measurements were performed. The normalized spectra taken at different incidence angles θ are presented in Fig. 9. Their overall shape is comparable to previous reports [10, 11, 15, 70]. The apparent strong dichroism in the spectra shows that the film exhibits

14

a preferential molecular alignment. The spectral contribution in the region below 290 eV stems exclusively from π^*-transitions. Above 293 eV, the spectrum is dominated by σ^*-transitions. The opposite behavior, i.e., increase (decrease) of the peaks intensities within the π^* region (σ^* region) for larger incident angles suggests molecules closer to an edge-on (either side-on or upright-standing) adsorption geometry.

For further analysis, we derived the π^*-related intensity by determining the spectral region below 286.5 eV. Fig. 9 b) shows these intensities and the corresponding fit according to Eq. (1), yielding $\alpha = 76\pm2°$. To visualize the significance of this result, Fig. 9 b) also includes the expected curves for Tc I (bulk, $\alpha = 74.5°$[5]) [34] and Tc II (thin film, $\alpha = 85.4°$) [23]. Taking into account the experimental error margins, the nominally 1 nm-thick *ultrathin* Tc film at H-Si(111) grown and measured at LT is in very good agreement with the Tc I (bulk)-derived curve, much better than with the curve for Tc II (thin film), rendering the inclination of the first Tc monolayer to resemble that of Tc I (bulk). This observation is in line with the DFT total energy calculations (reported in the previous section) that yield a Tc I-type monolayer ground state structure (see Fig. 3), although the measurements were performed at LT, whereas the calculations refer to zero temperature. It is known that the bulk Tc lattice constants show an anisotropic thermal expansion [71]. However, given the magnitude of the effect, we do not expect any qualitative changes of our predictions.

Tc films grown and measured at $T_{sub} = 265$ K

We prepared Tc thickness series on H-Si(111) as well as on a-Si:H at $T_{sub} = 265$ K, consisting of a sequence of Tc depositions and X-ray measurements performed contiguously on the same sample, with nominal coverages of 1, 2 and 3 nm on H-Si(111) (1 and 2 nm on a-Si:H). These substrates did not undergo any in-vacuum annealing and, thus, contain the full substrate-related carbon contribution

To derive the growth mode, we start with d derived for a nominal thickness of 1 nm. The d values reported in Table 2 – 1.15±0.4 nm for H-Si(111) and 1.3±0.4 nm for a-Si:H – agree rather well with the nominal thickness. However, Tc's complex growth mode and pronounced dewetting tendency [15, 16, 19] requires to analyze these d values and their evolution with nominal coverage with great care. Indeed, throughout the whole series, the relative intensity of all substrate-related signals are much more intense compared to those related to the LT case discussed above, evidencing that the different sample temperatures induce different growth modes. Fig. 10 presents the valence electron and NEXAFS C K-edge spectra, showing Tc- and substrate-related spectral weights of comparable magnitude. As expected, the Tc features become more prominent upon increasing the nominal Tc coverage. But the derived d-value, in contrast, decreases. This inverted behavior holds for both investigated substrates and allows assessing the vertical mass transport via the different mean escape depth (MED)[6] for d (1.4 – 1.7 nm, i.e., ~1.5 ML) and the valence electron and NEXAFS C K-edge spectra (0.6 – 1 nm i.e., ~1 ML). [43] Accordingly, the decrease of d can be explained by the fact that, upon deposition of additional Tc, second-layer molecules dewet and form thicker film regions that cover less area and contribute less spectral weight per molecule to

---

[5] The combined inclination angle α is given by Eq. (2) and not simply the arithmetic average of the individual values (69.48° and 81.87°) for the two molecules in the Tc bulk unit cell, which would be 75.7°.

[6] For hν = 700 eV, photoelectrons from the Si 2s (C 1s) core level have MED = 1.7 nm (1.4 nm). In contrast, photoelectrons from the valence region for hν = 153 eV (C KLL Auger electrons) have MED = 0.6 nm (1 nm; in the PEY mode, a fraction of the secondary electrons is also detected, enhancing the MED, but only to limited extend).

the XPS signal.[7] On the other hand, the increased Tc weight in the valence electron and NEXAFS C K-edge spectra evidences that, simultaneously, the proportion of surface area with film thickness ~1 ML increases. This demonstrates the stability of the first ML with regard to dewetting. Therefore, the Tc growth at $T_{sub} = 265$ K resembles the Stranski–Krastanov mode, as illustrated in Fig. 8 b). Note that at this temperature, we observed no dewetting during the NEXAFS measurements, showing that dewetting after growth is insignificant on the hour time scale.

Determining the π^*-related intensity for these samples required to employ a fitting routine that simultaneously accounts for Tc- and background-signal. The spectral shapes for the background and Tc species could be individually obtained from measurements of the substrates before Tc deposition and the Tc film deposited at LT, respectively. The spectral shapes feature characteristic peaks that enable robust fits. Examples for this fitting routine are shown in Figs. 11 a) and b). The α values for the thickness series, again determined by fitting Eq(1) to the intensity data, are included in Table 2.

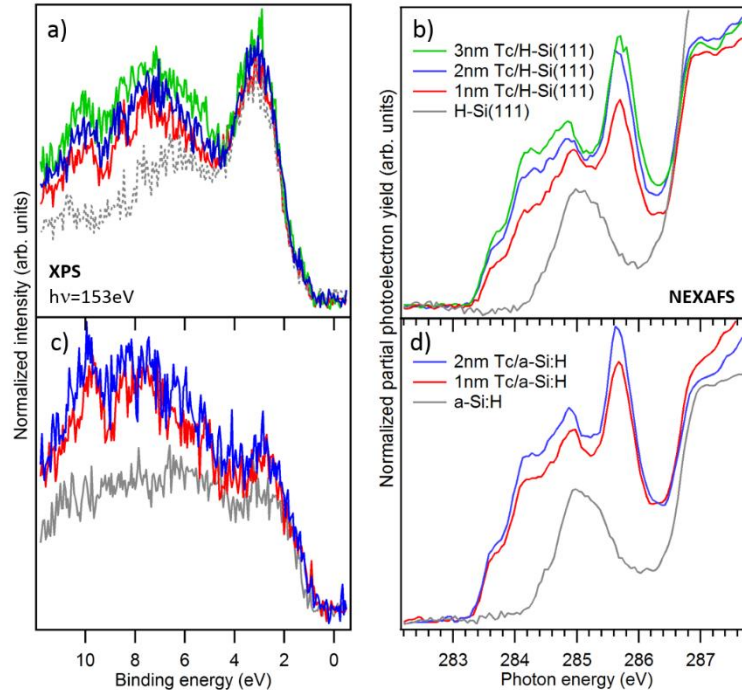**Figure 10**: Experimental spectra for the Tc thickness series on H-Si(111), deposited and measured at T_{sub}=265 K. a): Valence electron region; b): C K-edge NEXAFS. θ was 20° (30°) for the Tc films (the substrate-only spectrum). c,d): The same as a,b), but for a-Si:H substrate. All spectra have been scaled so that the intensity of the substrate contribution stays identical, as determined via fits (for C K-edge NEXAFS) and linear combination of substrate- and Tc-dominated spectra (for the valence electron region). The substrate-only spectrum in a) was not measured but derived by subtracting the Tc-contribution from the 1 nm Tc/H-Si(111) spectrum.

Room-temperature (RT) measurements of LT-deposited Tc films

Last but not least, we look at an ultrathin Tc film at $T_{sub} = $ RT in order to resolve possible temperature effects on the Tc orientation. To assess the corresponding film structure, we let the as-

---

[7] This behavior partly matches a previous report for Tc/SiO_2 that found that "with increasing deposition of Tc […] islands with less than three molecular layers are all subject to [...] mass transports from lower layers to higher layers." [16]. A similar behavior was also observed for a related COM [32].

deposited film (grown at LT) thermalize to RT over the course of 9 hours before re-analyzing it. Compared to the as-deposited film, the Si 2p (C 1s) signal in the XPS survey spectrum [see Fig. 7 a)] of the annealed film is significantly increased (decreased). The valence electron region is now clearly dominated by Si features [see Fig. 7 c)]]. These observations clearly show that at least parts of the RT-exposed H-Si(111) surface are now dramatically less covered by Tc molecules.

Further support for this scenario is given by the corresponding NEXAFS spectra [see Figs. 11 a) and b)]. A proper description requires much larger background contribution (BG) than those for the 265 K films. Since the latter films do not show significant spectral changes during several hours, the qualitative different Tc spectral weight cannot be explained by an aging effect. Instead we have to deduce that dewetting is significantly more pronounced for the room temperature film and also includes the first monolayer, thus representing a Volmer–Weber growth mode [*cf.* Fig 8 c)]. This sample indeed clearly showed a continued decrease of the Tc spectral weight in the NEXAFS spectra (40% in 100 minutes), evidencing Tc dewetting and possibly desorption almost linearly in time. This trend is accounted for in the data presented in Fig. 11 c) that yields $\alpha = 47.5\pm2°$ for the background signal (BG, originating from the carbon contamination of the substrate) and, most importantly, $\alpha = 63\pm2°$ for the Tc film. This is in line with previous reports in literature [10, 15] and also in accordance with the reduction of the inclination angle in less dense covered regions predicted by the DFT-calculations shown in Fig. 5. We will come back to this fact below.
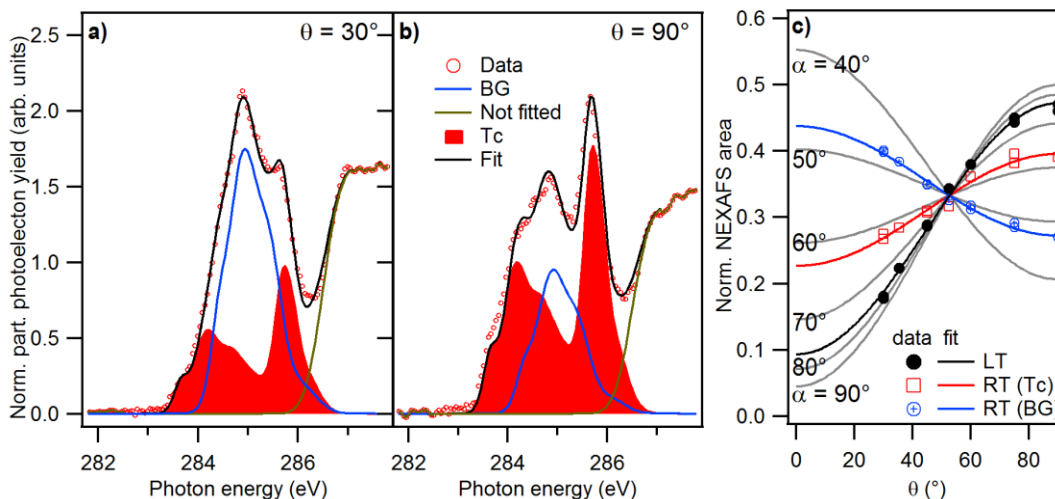

Figure 11: a, b): NEXAFS C K-edge spectra measured at $\theta = 30°$ and $\theta = 90°$ X-ray incidence, respectively, for 1 nm Tc at H-Si(111) grown at LT and heated to RT. The fitted spectral contributions from Tc and the substrate are also shown. c): π^* resonance intensities as a function of θ for the following signals: Tc measured at LT, Tc measured at RT, the residual substrate carbon (background, BG) signal at RT. Data shown with fits according to Eq.1, together with curves expected for some indicated α.

Calculated NEXAFS C K-edge for Tc adsorbate models

For further structure assessment, we provide DFT-calculated angle-dependent NEXAFS C K-edge spectra for reasonable model structures and compare them with the experimental spectra for the ultrathin film grown at LT. NEXAFS C K-edge spectra of single Tc molecules in '*gas phase*' (i.e. without intermolecular interaction) have been calculated before by Sueyoshi *et al.* [70] and Fratesi *et al.* [72]. The present calculations go beyond single-molecule spectra. Our NEXAFS spectra calculated for extended, 2D periodic structures, i.e. for the Tc I-type adsorbate and Tc I/Tc II crystalline structures, account for the influence of the substrate and intermolecular interactions.

17

The latter turn out to be predominantly responsible for the stability of the molecular Tc monolayer (see also the DFT-analysis above and Table 1).
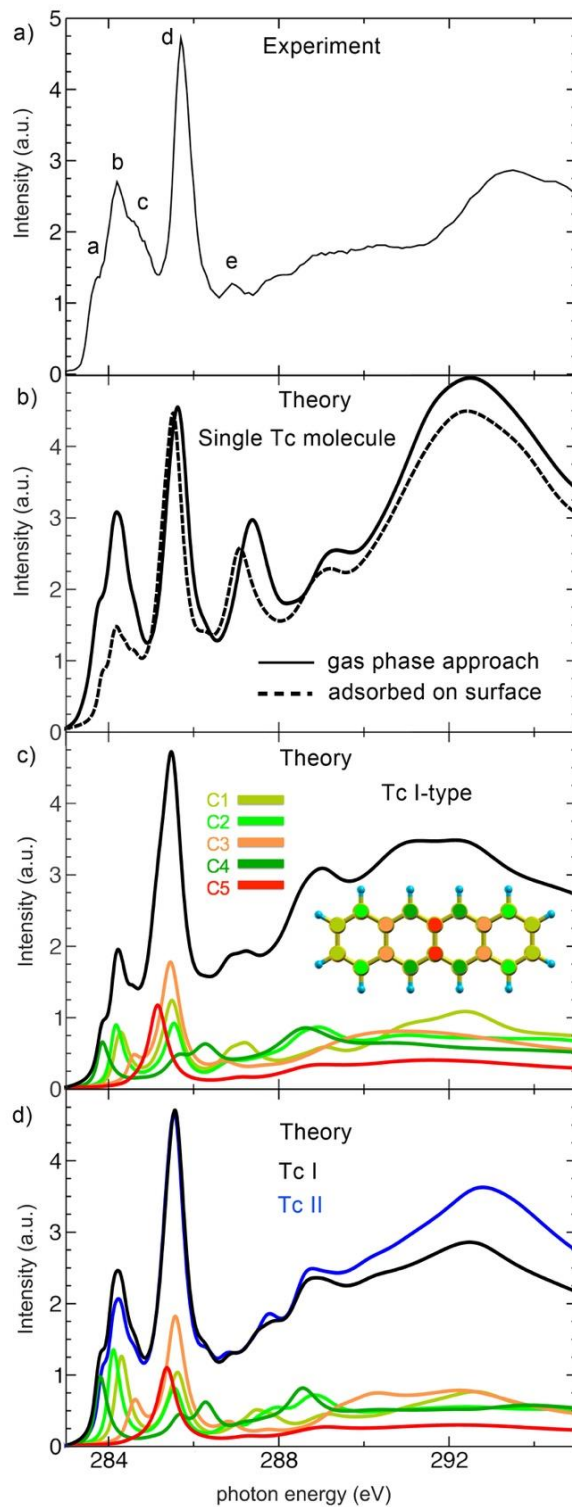

Figure 12: a): Experimental NEXAFS C K-edge spectrum of the LT film, shown exemplary at the incident angle $\theta =$ 52.5°. b), c) and d): DFT-calculated NEXAFS C K-edge spectrum for b) single Tc molecule in gas phase/vacuum (solid line) and adsorbed on surface (dashed), c) the most stable Tc monolayer structure (Tc I-type shown in Fig. 3) and d): the crystalline bulk-phase (black) and the crystalline thin-film phase (blue), respectively. All calculated spectra are also shown at incident angle $\theta = 52.5°$. In c) and d), the contributions of different C-atom types to the overall

18

spectrum of the Tc I-type and Tc I (bulk) are also shown (bottom). The inset shows the chemical structure of Tc and serves as reference for the color code. The binding energies and the relative intensities of the first five characteristic resonances are shown in Table 3.

Fig. 12 a) shows the experimental C K-edge NEXAFS spectrum for the LT film taken under incident angle $\theta = 52.5°$ [c.f. Fig. 9 a)]. In the energy range up to 286 eV (the π^* region), the first four peaks a, b, c, d are found at 283.75, 284.2, 284.55, and 285.7 eV, respectively. In the energy range above 286 eV, several broad resonances are superimposed to the ionization continuum forming a continuous structure of the spectra. In the energy range 287-292 eV, the spectrum shows almost constant intensity, while the intensity of the peak at 293.3 eV is about 60% of the main peak d.

Fig. 12 b) shows the corresponding calculated NEXAFS C K-edge spectra of the single Tc molecule in gas phase (solid line). It reproduces theoretical results of Fratesi *et al.* [72], and shows reasonable agreement with the experimental data, at least up to 286 eV. Above 287 eV, however, the calculated spectrum deviates considerably from the measurements. Here, strongly pronounced resonances appear at energies 287.4 and 292.5 eV. Whereas their energy can be somehow related to experiment, their intensity is drastically overestimated. Fig. 12 b) (dashed line) shows the spectrum of a single Tc molecule adsorbed on the surface (upright standing geometry). The resulting spectrum still features in many aspects the gas phase spectrum. The peak positions are slightly shifted, but only the position of the e peak fits better to the experimental spectrum. The intensities of the a, b, c peaks, however, provide even larger discrepancies with the measurements, e.g., the calculated intensity ratio b/d is 0.33, while it is 0.58 in the experiment. Single molecule approaches with and without substrate are, thus, quite far away from being representative of the measured ultrathin Tc films. Obviously, the deviations obtained are not related to the influence of the substrate, but to the absence of the intermolecular interactions as it will be shown in the following.

Fig. 12 c) shows the spectrum calculated for the Tc I-type structure (see also Fig. 3), which accounts for both the substrate and intermolecular interactions. Indeed, the spectrum now shows better agreement with the experiment. The calculated energies of the characteristic a-e peaks coincide within 0.05 eV with the experimental data, and the intensity of the formerly overestimated e peak and the broad resonance around 292 eV are now correctly reproduced. However, the binding energies above 288 eV as well as the intensities of the a, b, c peaks are still underestimated; i.e., the calculated intensity ratio b/d is only slightly increased to 0.4. Whereas the deviations above 288 eV might be related to the employed semi-local exchange-correlation functionals or to possible contributions from vibronic excitations to the final states [70], the deviations below 288 eV indicate some discrepancies between the modelled and measured structures. Our theoretical modelling assumes a perfect *single* monolayer of molecules in a direct contact with the substrate. The measured structure seems to deviate at least partially from this 1 ML assumption.

This argument is further supported by calculating the angle-dependent NEXAFS C K-edge spectra for the published XRD-derived crystal structures of bulk (Tc I) [34]. For comparison, the corresponding spectrum of thin-film Tc (Tc II) [20] is also shown. The calculated spectrum, especially for Tc I, is now in very good agreement with the experiment. The formerly underestimated characteristic peaks a, b, c are now almost identical to the measurements not only with respect to their binding energies, but also in terms of their shapes and intensities. Thereby, the first peak a results mainly from excitations of C4 carbon atoms into the lowest π^* orbitals (see decomposition of the spectrum into contributions from the five non-equivalent (C1 to C5) types of C atoms). Peak b is dominated by excitations from C1 and C2 carbon atoms. The feature c includes

contributions from C1, C2 and C3, whereas feature *d* carries contributions from all carbon types, but major contributions from the C=C carbon types (C3 and C5). Since the first two peaks (*a* and *b*) carry only contributions from the C-H carbon types, they are the mostly affected by the intermolecular interactions (compared to gas phase model) allowing their intensities to be close to the measurements. Apparently, Tc I fits much better to the measurement than Tc II. A *b/d* intensity ratio of 0.53 (Tc I) fairly agrees with the experimental data (0.58), whereas the calculated ratio for Tc II (0.46) appears much too small. Furthermore, the intensity of the Tc II resonances in the range above 289 eV are dramatically overestimated, whereas the Tc I curve perfectly reproduces the experimental intensity ratio of about 60 % of the main peak *d*. All-in-all, this supports *(i)* again the assumption of considerably tilted, preferential bulk phase-like molecular orientation in the first Tc monolayer(s) and *(ii)* that the closed ultrathin Tc film grown and measured at LT does not provide an entirely single monolayer, but contain residual regions with thickness > 1 ML.

Table 3. Binding energies and relative intensities of the first five NEXAFS resonances, calculated for the structural models of Tc shown in Fig. 12.

Binding energy [eV]/ Rel. intensity [% of peak *d*]	Peak *a*	Peak *b*	Peak *c*	Peak *d*	Peak *e*
Experiment	383.75/ 0.29	284.2/ 0.58	284.55/ 0.46	285.7/ 1	286.9/ 0.27
Single Tc in gas phase	283.80/ 0.40	284.2/ 0.66	284.60/ 0.39	285.7/ 1	286.4/ 0.33
Single Tc on the surface	283.85/ 0.18	284.2/ 0.33	284.60/ 0.25	285.5/ 1	286.2/ 0.31
Tc I-type	283.80/ 0.20	284.2/ 0.40	284.60/ 0.30	285.5/ 1	286.1/ 0.34
Tc I phase	283.80/ 0.28	284.2/ 0.53	284.60/ 0.33	285.6/ 1	286.2/ 0.31
Tc II phase	283.80/ 0.24	284.2/ 0.46	284.60/ 0.30	285.6/ 1	286.2/ 0.30

Comparative Discussion

Molecular orientation of ultrathin Tc films grown at LT and 265 K

From our NEXAFS data, the presence of a planar-oriented interlayer of molecules like in the case of pentacene on clean Si(001) [14] and α-Al$_2$O$_3$(0001) [73] can be safely excluded. Instead, the molecules in the ultrathin Tc film feature an orientation with average inclination angles between 76° and 78°. However, from NEXAFS alone it is not clear if the molecules are oriented with the molecular long axis (LA) closer to be parallel to the underlying surface or perpendicular to it (see Fig. 4). From all reports in literature (utilizing XRD, LEED, and AFM) [9, 10, 17, 19, 20, 23, 24, 26] as well as our own total energy calculations, we can safely assume an upright-standing Tc orientation.

As discussed in the *Results* section and illustrated in Fig. 8 a) and b), Tc growth at LT and 265 K resemble Frank–van der Merwe and Stranski–Krastanov modes, respectively. Accordingly, the LT film exhibits a closed first monolayer that is at least predominately covered by a second layer. In contrast, the thickness series grown at 265 K exhibit an incomplete and largely uncovered first monolayer. Despite these morphological differences, within the estimated uncertainty of ~2°, Tc-films for T_{sub} = 265 K and LT yielded the same *α*–value of approximately 77°. In addition, no significant coverage-dependent *α*-trend can be derived for the investigated ultrathin (1 − 3 ML thick) Tc films. Equally, the kind of substrate, crystalline H-Si(111) or amorphous a-Si:H, has no considerable influence on the molecular orientation.

The *α* values do not fully agree with pure bulk-like Tc I phase (74.5°). However, within the estimated error margin the Tc I angle fits much better than that expected for a thin film (Tc II)

phase (85.4°). This is in line with the better agreement of calculated NEXAFS spectra for the Tc I (bulk) crystal structures, and indicates that for as-deposited films, the orientation of the first ML clearly differs from that of the thin film regime. In other words, the ultrathin film regime, with 1 to ~3 ML, should be recognized as being distinct from the thin film regime (5 ML to 20 ML) [33]. In both transition regimes into the less inclined bulk-like Tc I phase, i.e. around 20 ML and for 3 – 4 ML, a mixture of both phases seems conceivable. Indeed, XRD measurements of Tc/H-Si(111) did resolve both phases for larger thicknesses [18].

Molecular orientation of Tc films after heating to RT

In the following we turn our attention to the film deposited at LT and later heated to RT. In this case, α is reduced to 63±2°, i.e., significantly lower than prior to annealing. This trend is opposite to that observed upon thermally activated erection of flat-lying polyacenes [9, 31, 32]. The resulting Tc inclination reflects several other observations in literature: upon stepwise Tc deposition onto H-Si(100) held at RT, $\alpha = 65±3°$ was derived from NEXAFS in the low coverage regime (nominally 1.2 ML) [15]. For > 3 ML coverage, α quickly converges to 78.4°, i.e., values similar to those observed for Tc films measured at $T_{sub} \leq 265$ K in the present work. Schedel *et al.* investigated Tc on oxidized Si(111) and reported the same trend towards lower α with decreasing coverage, but did not give a number for the low coverage regime [11]. For the (non-luminescent) disordered Tc films on AlO$_x$/Ni$_3$Al(111) grown at 100 K, upon annealing to 280 K, α of a multilayer film remains unaffected, but for 1 ML α changes from 43±5° to 63±5°.[10] The latter value is again identical to what we observed for the RT exposed sample in this work, and what was reported for RT grown Tc on H-Si(100) [15], suggesting a substrate-independent effect. Notably, the measurement of the annealed film on AlO$_x$/Ni$_3$Al(111) was performed with the sample again cooled to 100 K, indicating that the Tc structures with small inclination angle that emerge upon annealing are at least meta-stable.

All these findings indicate that at low coverages and ~RT, Tc molecules assemble into 1 ML islands that feature much smaller inclination angles than those known from the Tc I/II crystalline phases. A similar angle is reflected by the DFT calculated limit for Tc Ib-type, indicating less inclined, but still herringbone-like ordered (Tc-Ib type) monolayers (cf. Fig. 6 b,d) in the lowered coverage regime (see also Fig. 5). An accidental coincidence of all these α values is unlikely, and we have to take the α value of 63° seriously into account. Based on our DFT-analysis, we tentatively attribute the RT phase with $\alpha = 63°$ to a structure with an intermediate inclination similar to Tc Ib-type shown in Fig. 5 (bottom).

Conclusions

We elucidated the structure of ultrathin tetracene (Tc) films on H-passivated Si(111) and hydrogenated amorphous Si (a-Si:H) by combining NEXAFS and XPS experiments with DFT calculations. Our total energy calculations show that the stability of the Tc monolayer is predominantly due to intermolecular interaction, confirming that the lowest Tc layer is only weakly interacting with the substrate. This is also reflected by the calculated NEXAFS spectra. Whereas a periodic modelling of the molecular Tc layer is crucial for describing the experimentally observed spectra, the influence of the substrate is of minor importance. As a result, the gained knowledge on Tc-film growth can be safely transferred to any weakly interacting substrate and reasonably discussed based on published data obtained for similar substrates like H-Si(100) [15], oxidized Si(111) [11], or even AlO$_x$/Ni$_3$Al(111) [10].

In detail, ultrathin Tc films (≤ 3 ML) grown and measured at $T_{sub} \leq 265$ K are dominated by almost upright-standing, but still below $\alpha = 79°$ inclined molecules. The lowest monolayer, i.e. the molecules with direct contact to the substrate show a molecular packing almost identical to Tc bulk crystalline material, but with slightly different inclination angle (Tc I-type structure). The transition into the thin-film phase (Tc II) requires $2 - 4$ ML molecular material in order to decouple the deposited molecules completely from the weakly-interacting substrate. Finally, at film thicknesses of about $20 - 100$ ML the transition into the bulk-like Tc I phase takes place.

In contrast, ultrathin Tc films deposited at LT then heated to RT undergo a structural transformation, and exhibit a smaller α of about 63°. Based on a comparative analysis that includes observations for Tc on different weakly interacting surfaces, we suggest that both a low local coverage and a sufficiently high temperature are necessary conditions for the intermediate-inclination structure to appear, and that this structure is at least meta-stable. The larger overlap with the substrate wavefunctions makes this arrangement attractive for an optimized interfacial electron transfer in optoelectronic devices and solar cells. Hence, any condition (for example periodic heating and cooling or varying the growth rate) promoting the growth of more and larger islands, in the best case a perfect monolayer, with 63° inclined molecules appears to be beneficial for technological applications. We furthermore suggest following up the preparation of the RT-annealed ultrathin films by growing subsequent layers at decreased T_{sub} to stabilize the 63° Tc orientation at the interface against the structural transition around 3 ML that was observed for RT-grown samples.

Our structural information will enable energy-level alignment calculations for these hybrid interfaces along the lines of the work by Janke *et al.* published in parallel to ours [74].

Author Information

Corresponding Authors

*E-mail: jens.niederhausen@helmholtz-berlin.de

**E-mail: aldahhak@mail.uni-paderborn.de

‡These authors contributed equally.

Notes

The authors declare no competing financial interest.

Acknowledgements

beamline at HZB's synchrotron radiation facility BESSY II. Alexander Hinderhofer, Alexander Gerlach, and Frank Schreiber (University Tübingen) are acknowledged for insightful discussions.

References

1.	Einzinger, M.; Wu, T.; Kompalla, J. F.; Smith, H. L.; Perkinson, C. F.; Nienhaus, L.; Wieghold, S.; Congreve, D. N.; Kahn, A.; Bawendi, M. G.; Baldo, M. A. Sensitization of silicon by singlet exciton fission in tetracene. *Nature* **2019,** *571* (7763), 90-94.

2.	Piland, G. B.; Burdett, J. J.; Hung, T.-Y.; Chen, P.-H.; Lin, C.-F.; Chiu, T.-L.; Lee, J.-H.; Bardeen, C. J. Dynamics of molecular excitons near a semiconductor surface studied by fluorescence quenching of polycrystalline tetracene on silicon. *Chem. Phys. Lett.* **2014,** *601*, 33 - 38.

3.	MacQueen, R. W.; Liebhaber, M.; Niederhausen, J.; Mews, M.; Gersmann, C.; Jäckle, S.; Jäger, K.; Tayebjee, M. J. Y.; Schmidt, T. W.; Rech, B.; Lips, K. Crystalline silicon solar cells with tetracene interlayers: the path to silicon-singlet fission heterojunction devices. *Mater. Horiz.* **2018,** *5*, 1065-1075.

4.	Smith, M. B.; Michl, J. Singlet Fission. *Chem. Rev.* **2010,** *110* (11), 6891-6936.

5.	Dexter, D. L. Two ideas on energy transfer phenomena: Ion-pair effects involving the OH stretching mode, and sensitization of photovoltaic cells. *Journal of Luminescence* **1979,** *18-19*, 779 - 784.

6.	Rao, A.; Friend, R. H. Harnessing singlet exciton fission to break the Shockley-Queisser limit. *Nat. Rev. Mater.* **2017,** *2* (11), 17063.

7.	Dexter, D. L. A Theory of Sensitized Luminescence in Solids. *J. Chem. Phys.* **1953,** *21* (5), 836-850.

8.	Langner, A.; Su, Y.; Sokolowski, M. Luminescence quenching of tetracene films adsorbed on an ultrathin alumina AlO_x layer on $Ni_3Al(111)$. *Phys. Rev. B* **2006,** *74*, 045428.

9.	Soubatch, S.; Temirov, R.; Weinhold, M.; Tautz, F. S. The interplay between molecular orientation, film morphology and luminescence properties of tetracene thin films on epitaxial $AlO_x/Ni_3Al(111)$. *Surf. Sci.* **2006,** *600* (20), 4679-4689.

10.	Naboka, M.; Soubatch, S.; Nefedov, A.; Tautz, F. S.; Wöll, C. Direct Evidence of the Temperature-Induced Molecular Reorientation in Tetracene Thin Films on $AlO_x/Ni_3Al(111)$. *J. Phys. Chem. C* **2014,** *118* (39), 22678-22682.

11.	Schedel, T.; Frank, K.-H.; Karlsson, U.; Koch, E. E. Orientation of tetracene as a large hydrocarbon on Si(111)-(7 x 7) and oxidized Si(111). *Vacuum* **1990,** *41* (1), 652 - 655.

12.	Yong, K. S.; Zhang, Y. P.; Yang, S.-W.; Wu, P.; Xu, G. Q. Studies of Chemisorbed Tetracene on Si(111)-7x7. *J. Phys. Chem. A* **2007,** *111* (49), 12266-12274.

13.	Rada, T.; Chen, Q.; Richardson, N. V. Scanning tunnelling microscopy of tetracene on Si(100)-2x1. *J. Phys.: Condens. Matter* **2003,** *15* (38), S2749-S2756.

14.   zu Heringdorf, F.-J. M. The application of low energy electron microscopy and photoemission electron microscopy to organic thin films. *J. Phys.: Condens. Matter* **2008,** *20* (18), 184007.

15.   Tersigni, A.; Shi, J.; Jiang, D. T.; Qin, X. R. Structure of tetracene films on hydrogen-passivated Si(001) studied via STM, AFM, and NEXAFS. *Phys. Rev. B* **2006,** *74*, 205326.

16.   Shi, J.; Qin, X. R. Nucleation and growth of tetracene films on silicon oxide. *Phys. Rev. B* **2008,** *78*, 115412.

17.   Tersigni, A.; Qin, X. R.; Kim, C.-Y.; Gordon, R. A.; Jiang, D. T. Reciprocal-space mapping of lateral single-crystal domains with grazing-incidence x-ray diffraction for tetracene on H/Si(001). *Phys. Rev. B* **2011,** *84*, 035303.

18.   Liebhaber, M. L. Silicon heterojunction solar cells: From conventional concepts to a singlet fission multi-exciton generating hybrid approach. PhD thesis, 2017.

19.   Shi, J.; Qin, X. R. Flux dependence of the morphology of a tetracene film on hydrogen-passivated Si(100). *Phys. Rev. B* **2006,** *73*, 121303.

20.   Tersigni, A.; Sadowski, J. T.; Qin, X.-R. Visualization of molecular packing and tilting domains and interface effects in tetracene thin films on H/Si(001). *Phys. Status Solidi B* **2017,** *254* (7), 1600777.

21.   Milita, S.; Servidori, M.; Cicoira, F.; Santato, C.; Pifferi, A. Synchrotron X-ray investigation of tetracene thin films grown at different deposition fluxes. *Nucl. Instrum. Methods Phys. Res. B* **2006,** *246* (1), 101-105.

22.   Gompf, B.; Faltermeier, D.; Redling, C.; Dressel, M.; Pflaum, J. Tetracene film morphology: Comparative atomic force microscopy, X-ray diffraction and ellipsometry investigations. *Eur. Phys. J. E* **2008,** *27* (4), 421-424.

23.   Pithan, L.; Nabok, D.; Cocchi, C.; Beyer, P.; Duva, G.; Simbrunner, J.; Rawle, J.; Nicklin, C.; Schäfer, P.; Draxl, C.; Schreiber, F.; Kowarik, S. Molecular structure of the substrate-induced thin-film phase of tetracene. *J. Chem. Phys.* **2018,** *149* (14), 144701.

24.   Arias, D. H.; Ryerson, J. L.; Cook, J. D.; Damrauer, N. H.; Johnson, J. C. Polymorphism influences singlet fission rates in tetracene thin films. *Chem. Sci.* **2016,** *7*, 1185-1191.

25.   Nahm R., K.; Engstrom J., R. Unexpected Effects of the Rate of Deposition on the Mode of Growth and Morphology of Thin Films of Tetracene Grown on SiO_2. *J. Phys. Chem. C* **2016,** *120*, 7183.

26.   Pithan, L.; Beyer, P.; Bogula, L.; Zykov, A.; Schäfer, P.; Rawle, J.; Nicklin, C.; Opitz, A.; Kowarik, S. Direct Photoalignment and Optical Patterning of Molecular Thin Films. *Adv. Mater.* **2017,** *29* (6), 1604382.

27.   Wünsche, J.; Tarabella, G.; Bertolazzi, S.; Bocoum, M.; Coppedè, N.; Barba, L.; Arrighetti, G.; Lutterotti, L.; Iannotta, S.; Cicoira, F.; Santato, C. The correlation between gate

dielectric, film growth, and charge transport in organic thin film transistors: the case of vacuum-sublimed tetracene thin films. *J. Mater. Chem. C* **2013,** *1*, 967.

28. Milita, S.; Santato, C.; Cicoira, F. Structural investigation of thin tetracene films on flexible substrate by synchrotron X-ray diffraction. *Appl. Surf. Sci.* **2006,** *252* (22), 8022.

29. Eiermann, R.; Parkinson, G. M.; Bässler, H.; Thomas, J. M. Structural investigations of amorphous tetracene and pentacene by low-temperature electron diffraction. *J. Phys. Chem.* **1983,** *87* (4), 544-551.

30. Hasegawa, S.; Inokuchi, H.; Seki, K.; Ueno, N. Angle-resolved photoemission from oriented thin films of naphthacene: comparison with theoretical spectra. *J. Electron Spectrosc. Relat. Phenom.* **1996,** *78*, 391-394.

31. Bussolotti, F.; Han, S. W.; Honda, Y.; Friedlein, R. Phase-dependent electronic properties of monolayer and multilayer anthracene films on graphite [0001] surfaces. *Phys. Rev. B* **2009,** *79*, 245410.

32. Niederhausen, J.; Duhm, S.; Bürker, C.; Xin, Q.; Vollmer, A.; Schreiber, F.; Kera, S.; Ueno, N.; Koch, N. Temperature dependent growth and dewetting behavior of tetraseleno-tetracene on Au(111) and Ag(111) studied by photoelectron spectroscopy. 2013.

33. Nahm, R. K.; Engstrom, J. R. Who's on first? Tracking in real time the growth of multiple crystalline phases of an organic semiconductor: Tetracene on SiO_2. *J. Chem. Phys.* **2017,** *146* (5), 052815.

34. Holmes, D.; Kumaraswamy, S.; Matzger A., J.; Vollhardt K. P., C. On the Nature of Nonplanarity in the [N]Phenylenes. *Chem. Eur. J.* **1999,** *5*, 3399.

35. Breuer, T.; Klues, M.; Witte, G. Characterization of Orientational Order in π-conjugated Molecular Thin Films by NEXAFS. *J. Electron Spectrosc. Relat. Phenom.* **2015,** *204*, 102 - 115.

36. Sondermann, U.; Kutoglu, A.; Bässler, H. X-ray diffraction study of the phase transition in crystalline tetracene. *J. Phys. Chem.* **1985,** *89* (9), 1735-1741.

37. Breuer, T.; Salzmann, I.; Götzen, J.; Oehzelt, M.; Morherr, A.; Koch, N.; Witte, G. Interrelation between Substrate Roughness and Thin-film Structure of Functionalized Acenes on Graphite. *Cryst. Growth Des.* **2011,** *11*, 4996.

38. Stöhr, J.; Outka, D. A. Determination of molecular orientations on surfaces from the angular dependence of near-edge x-ray-absorption fine-structure spectra. *Phys. Rev. B* **1987,** *36*, 7891-7905.

39. Nefedov, A.; Wöll, C. Advanced Applications of NEXAFS Spectroscopy for Functionalized Surfaces. In *Surface Science Techniques*, Bracco, G.; Holst, B., Eds.; Springer Berlin Heidelberg: Berlin, Heidelberg, 2013, pp 277-303.

40. Yeh, J. J. Atomic Calculation of Photoionization Cross-Sections and Asymmetry Parameters. In *Surface Science Techniques*; Gordon and Breach Science Publishers: Langhorne, PE (USA), 1993 (data retrieved via https://vuo.elettra.eu/services/elements/WebElements.html).

41.   Hubbard, C. R.; Swanson, H. E.; Mauer, F. A. A silicon powder diffraction standard reference material. *J. Appl. Crystallogr.* **1975,** *8* (1), 45-48.

42.   Drera, G.; Salvinelli, G.; Åhlund, J.; Karlsson, P. G.; Wannberg, B.; Magnano, E.; Nappini, S.; Sangaletti, L. Transmission function calibration of an angular resolved analyzer for X-ray photoemission spectroscopy: Theory vs experiment. *J. Electron. Spectrosc. Relat. Phenom.* **2014,** *195*, 109 - 116.

43.   Powell, C. J.; Jablonski, A. NIST Electron Effective-Attenuation-Length Database - Version 1.3. National Institute of Standards and Technology, Gaithersburg, MD, 2011.

44.   Giannozzi, P.; Baroni, S.; Bonini, N.; Calandra, M.; Car, R.; Cavazzoni, C.; Ceresoli, D.; Chiarotti, G. L.; Cococcioni, M.; Dabo, I.; Corso, A. D.; de Gironcoli, S.; Fabris, S.; Fratesi, G.; Gebauer, R.; Gerstmann, U.; Gougoussis, C.; Kokalj, A.; Lazzeri, M.; Martin-Samos, L.; Marzari, N.; Mauri, F.; Mazzarello, R.; Paolini, S.; Pasquarello, A.; Paulatto, L.; Sbraccia, C.; Scandolo, S.; Sclauzero, G.; Seitsonen, A. P.; Smogunov, A.; Umari, P.; Wentzcovitch, R. M. QUANTUM ESPRESSO: a modular and open-source software project for quantum simulations of materials. *J. Phys.: Condens. Matter* **2009,** *21* (39), 395502.

45.   Perdew, J. P.; Burke, K.; Ernzerhof, M. Generalized Gradient Approximation Made Simple. *Phys. Rev. Lett.* **1996,** *77*, 3865-3868.

46.   Ortmann, F.; Bechstedt, F.; Schmidt, W. G. Semiempirical van der Waals correction to the density functional description of solids and molecular structures. *Phys. Rev. B* **2006,** *73*, 205101.

47.   Taillefumier, M.; Cabaret, D.; Flank, A.-M.; Mauri, F. X-ray absorption near-edge structure calculations with the pseudopotentials: Application to the K edge in diamond and α-quartz. *Phys. Rev. B* **2002,** *66*, 195107.

48.   Gougoussis, C.; Calandra, M.; Seitsonen, A. P.; Mauri, F. First-principles calculations of x-ray absorption in a scheme based on ultrasoft pseudopotentials: From α-quartz to high-T_c compounds. *Phys. Rev. B* **2009,** *80*, 075102.

49.   Aldahhak, H.; Paszkiewicz, M.; Rauls, E.; Allegretti, F.; Tebi, S.; Papageorgiou, A. C.; Zhang, Y.-Q.; Zhang, L.; Lin, T.; Paintner, T.; Koch, R.; Schmidt, W. G.; Barth, J. V.; Schöfberger, W.; Müllegger, S.; Klappenberger, F.; Gerstmann, U. Identifying On-Surface Site-Selective Chemical Conversions by Theory-Aided NEXAFS Spectroscopy: The Case of Free-Base Corroles on Ag(111). *Chem. Eur. J.* **2018,** *24* (26), 6787-6797.

50.   Aldahhak, H.; Paszkiewicz, M.; Allegretti, F.; Duncan, D. A.; Tebi, S.; Deimel, P. S.; Casado Aguilar, P.; Zhang, Y.-Q.; Papageorgiou, A. C.; Koch, R.; Barth, J. V.; Schmidt, W. G.; Müllegger, S.; Schöfberger, W.; Klappenberger, F.; Rauls, E.; Gerstmann, U. X-ray Spectroscopy of Thin Film Free-Base Corroles: A Combined Theoretical and Experimental Characterization. *J. Phys. Chem. C* **2017,** *121* (4), 2192-2200.

51.   Buczko, R.; Duscher, G.; Pennycook, S. J.; Pantelides, S. T. Excitonic Effects in Core-Excitation Spectra of Semiconductors. *Phys. Rev. Lett.* **2000,** *85*, 2168-2171.

52.   Lanczos, C. Solution of systems of linear equations by minimized iterations. *J. Res. Natl. Bur. Stand.* **1952,** *49*, 33-53.

53.   Haydock, R.; Heine, V.; Kelly, M. J. Electronic structure based on the local atomic environment for tight-binding bands. II. *J. Phys. C: Solid State Phys.* **1975,** *8* (16), 2591-2605.

54.   Walker, B.; Gebauer, R. Ultrasoft pseudopotentials in time-dependent density-functional theory. *J. Chem. Phys.* **2007,** *127* (16), 164106.

55.   Gaudry, E.; Cabaret, D.; Brouder, C.; Letard, I.; Rogalev, A.; Wilhlem, F.; Jaouen, N.; Sainctavit, P. Relaxations around the substitutional chromium site in emerald: X-ray absorption experiments and density functional calculations. *Phys. Rev. B* **2007,** *76*, 094110.

56.   Juhin, A.; Brouder, C.; Arrio, M.-A.; Cabaret, D.; Sainctavit, P.; Balan, E.; Bordage, A.; Seitsonen, A. P.; Calas, G.; Eeckhout, S. G.; Glatzel, P. X-ray linear dichroism in cubic compounds: The case of Cr^{3+} in $MgAl_2O_4$. *Phys. Rev. B* **2008,** *78*, 195103.

57.   Cabaret, D.; Mauri, F.; Henderson, G. S. Oxygen K-edge XANES of germanates investigated using first-principles calculations. *Phys. Rev. B* **2007,** *75*, 184205.

58.   Ehlert, C.; Unger, W. E. S.; Saalfrank, P. C K-edge NEXAFS spectra of graphene with physical and chemical defects: a study based on density functional theory. *Phys. Chem. Chem. Phys.* **2014,** *16*, 14083-14095.

59.   S. García-Gil, A. G.; Ordejón, P. Calculation of core level shifts within DFT using pseudopotentials and localized basis sets. *The European Physical Journal B* **2012,** *85*, 239.

60.   Bunău, O.; Calandra, M. Projector augmented wave calculation of x-ray absorption spectra at the $L_{2,3}$ edges. *Phys. Rev. B* **2013,** *87*, 205105.

61.   Rignanese, G.-M.; Pasquarello, A. Nitrogen 1s core-level shifts at the NH3 saturated Si(100)-2x1 surface: a first-principles study. *Surf. Sci.* **2001,** *490* (1), L614 - L618.

62.   Rignanese, G.-M.; Pasquarello, A. Nitrogen bonding configurations at nitrided Si(001) surfaces and Si(001)-SiO_2 interfaces: A first-principles study of core-level shifts. *Phys. Rev. B* **2001,** *63*, 075307.

63.   Tebi, S.; Paszkiewicz, M.; Aldahhak, H.; Allegretti, F.; Gonglach, S.; Haas, M.; Waser, M.; Deimel, P. S.; Aguilar, P. C.; Zhang, Y.-Q.; Papageorgiou, A. C.; Duncan, D. A.; Barth, J. V.; Schmidt, W. G.; Koch, R.; Gerstmann, U.; Rauls, E.; Klappenberger, F.; Schöfberger, W.; Müllegger, S. On-Surface Site-Selective Cyclization of Corrole Radicals. *ACS Nano* **2017,** *11* (3), 3383-3391.

64.   Aldahhak, H.; Powroźnik, P.; Pander, P.; Jakubik, W.; Dias, F. B.; Schmidt, W. G.; Gerstmann, U.; Krzywiecki, M. Toward Efficient Toxic-Gas Detectors: Exploring Molecular Interactions of Sarin and Dimethyl Methylphosphonate with Metal-Centered Phthalocyanine Structures. *J. Phys. Chem. C* **2020,** *124* (11), 6090-6102.

65.   Bunău, O.; Joly, M. Self-consistent aspects of x-ray absorption calculations. *J. Phys.: Condens. Matter* **2009,** *21* (34), 345501.

66.   Jakob, P.; Menzel, D. Initial stages of multilayer growth and structural phase transitions of physisorbed benzene on Ru(001). *J. Chem. Phys.* **1996,** *105* (9), 3838-3848.

67.   Kaefer, D.; Bashir, A.; Witte, G. Interplay of Anchoring and Ordering in Aromatic Self-Assembled Monolayers. *J. Phys. Chem. C* **2007,** *111* (28), 10546-10551.

68.   Bröker, B.; Hofmann, O. T.; Rangger, G. M.; Frank, P.; Blum, R. P.; Rieger, R.; Venema, L.; Vollmer, A.; Müllen, K.; Rabe, J. P.; Winkler, A.; Rudolf, P.; Zojer, E.; Koch, N. Density-Dependent Reorientation and Rehybridization of Chemisorbed Conjugated Molecules for Controlling Interface Electronic Structure. *Phys. Rev. Lett.* **2010,** *104* (24), 246805.

69.   Graber, T.; Forster, F.; Schöll, A.; Reinert, F. Experimental determination of the attenuation length of electrons in organic molecular solids: The example of PTCDA. *Surf. Sci.* **2011,** *605* (9--10), 878-882.

70.   Sueyoshi, T.; Willenbockel, M.; Naboka, M.; Nefedov, A.; Soubatch, S.; Wöll, C.; Tautz, F. S. Spontaneous Change in Molecular Orientation at Order-Disorder Transition of Tetracene on Ag(111). *J. Phys. Chem. C* **2013,** *117* (18), 9212-9222.

71.   Haas, S.; Batlogg, B.; Besnard, C.; Schiltz, M.; Kloc, C.; Siegrist, T. Large uniaxial negative thermal expansion in pentacene due to steric hindrance. *Phys. Rev. B* **2007,** *76* (20), 205203.

72.   Fratesi, G.; Lanzilotto, V.; Floreano, L.; Brivio, G. P. Azimuthal Dichroism in Near-Edge X-ray Absorption Fine Structure Spectra of Planar Molecules. *J. Phys. Chem. C* **2013,** *117* (13), 6632-6638.

73.   Zhang, L.; Fu, X.; Hohage, M.; Zeppenfeld, P.; Sun, L. D. Growth of pentacene on α-Al_2O_3(0001) studied by in situ optical spectroscopy. *Phys. Rev. Materials* **2017,** *1*, 043401.

74.   Janke, S. M.; Rossi, M.; Levchenko, S. V.; Kokott, S.; Scheffler, M.; Blum, V. Pentacene and Tetracene Molecules and Films on H/Si(111): Level Alignment from Hybrid Density Functional Theory. *Electron. Struct.* **2020,** https://doi.org/10.1088/2516-1075/ab9bb5.

For Table of Contents Use Only